Chapter 12
Towards Molecular Movies of Enzymes

Christopher Kupitz and Marius Schmidt

12.1 Introduction

Biological macromolecules can be thought of as molecular machines. The components of these machines are in constant motion, even in their "rest" states. This constant motion causes structural heterogeneity visible in high resolution measurements [1], revealed as regions of disorder or as multiple conformations. The nature and relevance of this heterogeneity and its underlying fluctuations is of large scientific interest, and it is widely investigated as they have functional importance [1–5]. In order to understand macromolecular function, "static" structures are simply not sufficient. As a reaction proceeds, the macromolecular structure has to change in order to promote function. The determination of both structure and dynamics is possible through the use of time-resolved crystallography [6–9]. This requires that a reaction is triggered successfully inside crystals. For this to be feasible, the duration of reaction initiation must be significantly shorter than the fastest process of interest in the biomolecule. If time-resolved methods are not applicable, reactions can be examined on longer time scales. Molecules can accumulate into a steady state regime [10] or they can be trapped in intermediate states by lowering the temperature [11]. For example, trap-freeze is a technique in which a reaction in a crystal is started at room temperature, and the crystal is subsequently flash frozen after a targeted intermediate state has been occupied. The introduction of amino acid mutations into the protein may also be an effective method to trap intermediates [12]. However, the time-scale of the population formation and its decay is lost.

C. Kupitz (✉) · M. Schmidt
Physics Department, University of Wisconsin-Milwaukee, Milwaukee, WI, USA
e-mail: kupitz@uwm.edu; smarius@uwm.edu

S. Boutet et al. (eds.), *X-ray Free Electron Lasers*,
https://doi.org/10.1007/978-3-030-00551-1_12

The goal of time-resolved crystallography is to create a "movie" of reacting protein molecules, which proceed along a reaction pathway. Using the term "movie" can be slightly misleading, so it is important to understand what type of information is actually being obtained. Rather than showing the trajectory of the molecules in the ensemble, it shows a population increase or decrease in a succession of intermediate states along the reaction pathway. An example of a chemical kinetic mechanism of a reaction catalyzed by an enzyme is shown below:

$$\mathrm{E} + \mathrm{S} \underset{k_{-1}}{\overset{k_1}{\rightleftarrows}} \mathrm{ES} \overset{k_2}{\rightarrow} \mathrm{EP} \overset{k_3}{\rightarrow} \mathrm{E} + \mathrm{P}$$

To start this reaction, the free enzyme (E), is mixed with substrate (S). The substrate binds to the enzyme forming the enzyme-substrate complex (ES). Here, k_1 is a second order rate coefficient for the binding, while k_{-1} accounts for the dissociation of ES. The reaction then proceeds along the catalytic pathway leading to an enzyme-product (EP) complex. Finally, free enzyme (E) is recovered, and the product (P) is released. ES and EP are reaction intermediates while k_2 and k_3 are first order rate coefficients.

A reaction can also be successfully triggered by light provided that a photosensitive group (a chromophore) is bound to the protein. After activation, the molecules within the crystal travel along the reaction pathway and may occupy intermediate states. Intermediate states correspond to local energy minima in configurational space [13–15] (See Fig. 12.1a). Intermediate states are characterized by distinct structures. In Fig. 12.1a, two intermediates denoted as I_1 and I_2 are shown. Molecules only briefly (transiently) populate these states before moving on to the next state. Structures of the intermediate states can only be determined when they are occupied by reacting molecules. To determine their structures, the concentrations of molecules in these states must build up to detectable levels. Even if the chemical kinetic mechanism allows for a sufficient buildup in a particular intermediate state, other intermediate states are occupied at the same time, hence they might mix in. There might, however, exist time points where only a single intermediate is occupied. Moreover, there might be periods of time when concentrations of molecules in intermediate states do not change (see Fig. 12.1). Then a single time point may be sufficient to determine the structure of an intermediate. In general, however, multiple intermediates contribute to any point in time, and methods for deconvoluting the X-ray data into pure constituents are needed in order to determine the individual structures [17, 18]. In contrast to intermediate states, transition states are located at the top of the barriers of activation; an example is shown in Fig. 12.1b. A protein molecule may pass from one minimum to another minimum by acquiring sufficient energy from the thermal bath to surmount this barrier. Transition states are only visited very shortly. Molecules do not persist there long enough that they can accumulate sufficiently (build up sufficient occupancy) for time-resolved experiments to detect them.

Synchrotron-based time-resolved crystallography has been highly successful at elucidating cyclic (reversible) reactions, which are activated by short light pulses

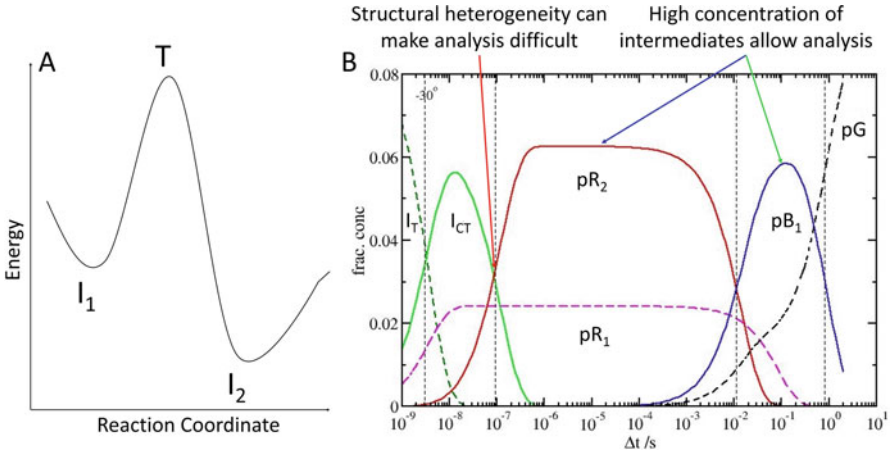

Fig. 12.1 Chemical kinetics. (**a**) Diagram of intermediate states with the energy minima corresponding to intermediate states (I_1 and I_2) and the transitional state (T) at the peak of the activation barrier. Reaction coordinate can refer to many variables such as distance, or torsional angle. (**b**) Time-dependent concentrations as determined for Photoactive Yellow Protein at −30 °C [16]. The red arrow indicates a time point where several intermediate states are occupied at the same time (I_{CT}, pR_1, and pR_2). The blue arrow points out a time regime where the concentration of molecules in two intermediate states does not change. Since the time dependence of pR_1 and pR_2 are similar it is difficult to separate them using the time information. The green arrow shows a point in time where only one intermediate is occupied (pB_1). The structure of this intermediate can be solved at this time point

[16, 19–27], but irreversible (non-cyclic) reactions are a challenge to study at synchrotrons. A major difficulty lies in having to reset the reaction before every X-ray pulse in order to ensure an accumulation of signal from a single X-ray pulse. While light activated reactions can also be non-cyclic, many of the interesting systems that contain irreversible processes do not involve light sensitive molecules. This implies that general methods to start reactions other than by light activation are developed. With the appearance of the first free electron lasers (FELs) for hard X-rays, time-resolved crystallography is on the verge of a revolution [28–32], which opens the door to optically and non-optically triggered non-cyclic (single path) reactions. Several prominent features of X-ray FELs promote a new paradigm for time-resolved crystallography: (1) The "diffraction-before-destruction" principle [33] states that the X-ray pulses are so short that a diffraction pattern is collected before radiation damage destroys the sample [28, 29, 34]. Early SFX experiments have demonstrated that the data sets are essentially free of radiation damage [28]. (2) The high intensity allows the use of micron-sized crystals that are exposed to the X-ray pulse only once at a given time delay, a requirement to investigate irreversible reactions. Crystals are injected in random orientations as a serial data collection strategy is employed [29, 30, 32, 35, 36]. (3) Micron-sized crystals make it easier to excite the sample consistently with light or trigger the reaction chemically by diffusion based methods. (4) The ultrafast pulses allow the crystallographic data to

be collected at ambient (i.e., biologically relevant) temperatures [37], and (5) the fs X-ray pulses available at the X-ray FEL, as opposed to the 100 ps pulse duration at synchrotrons, improves the time-resolution that can be achieved, if needed.

12.2 Reaction Initiation

The ability to trigger or initiate a reaction is essential for any time-resolved experiment. The reaction initiation must occur essentially simultaneously across as many molecules as possible in a crystal. In addition, the trigger must be significantly shorter than the lifetime of the intermediates of interest. A number of methods can be employed to trigger reactions (Table 12.1), and two methods are widely used: light activation and chemical activation via adding substrates, ligands, and other small molecules. Reaction initiation techniques can cause large structural changes, which might compromise crystal integrity. For example, crystals of the Photosystem I–ferredoxin complex quickly fall apart upon light excitation [35, 42]. Therefore, these experiments are particularly difficult to perform at synchrotrons, when multiple pump–probe sequences on the same crystal are required to produce a single diffraction pattern. At the X-ray FEL, however, experiments are performed in a different way. (1) Microcrystals are used, which might support larger structural changes. (2) The experiment is not impaired if the crystal fails or cracks after the single shot measurement, because crystal cracking takes longer than most time-points of interest. As a consequence, the dynamics can be measured up to the time point where the crystal is falling apart (see below).

12.2.1 Activation by Light

Reaction initiation by short laser pulses provides undoubtedly the highest temporal resolution for time-resolved crystallography. The photo-dissociation and rebinding of CO to heme proteins [26, 43], and the isomerization of the photoactive yellow protein (PYP) chromophore from trans to cis [19] are both examples. Both

Table 12.1 Methods of reaction initiation in protein crystals

Method	Time resolution	Experimental complexity
Light driven proteins [31]	Ultrafast, ~100–280 fs achievable	Low
Caged substrates, macrocrystallography [38]	>100 ns	High
Diffusive mixing, serial crystallography [39, 40]	~100 μs	Low
Electric fields, temperature jump, etc. [41]	Variable but typically moderate	Variable

myoglobin and PYP were essential to develop new techniques in time-resolved crystallography [16, 18, 20, 22, 23, 25, 26, 31, 32, 44–50]. Protein macrocrystals contain between 10^{13} and 10^{14} individual protein molecules, depending on the size and the packing in the crystal. The optical density in the absorption region of the chromophore is unusually high due to the tight packing of molecules in a crystal. Consequently, the penetration depth into a crystal can be very small, on the order of a few micrometers [16, 32]. Therefore, wavelength and illumination geometry have to be carefully considered [32]. Microcrystals are clearly advantageous as the optical path through a microcrystal is, by definition, small. This allows the excitation wavelength to be closer to the absorption maximum, which results in a more effective reaction initiation [51, 52]. However, the laser peak power needs to be carefully selected. Too high a laser power could lead to damaging effects such as two photon absorption and radical formation, especially when ultrashort laser pulses are used. In contrast, if the laser power is too low, not enough molecules are excited and the occupation of molecules in intermediate states might be too small to be detected. A broad range of laser pulse energy densities have been used, typically ranging from 0.5–5 mJ/mm^2. This should be tailored to the individual protein and experiment for best results, by examining the reaction spectroscopically ahead of time [30, 32, 35, 43].

12.2.2 Activation by Caged Substrates

The majority of proteins are not naturally photosensitive. In these cases, there are other options that need to be explored to trigger the protein dynamics. Photoreactive caged substrates, also known as photoactivatable bio-agents can be used. These agents are composed of small molecules and compounds, for example a cofactor, substrate, or even a protein residue, which has been chemically inactivated by a photosensitive protecting group [11, 53, 54]. Oxygen, phosphate, adenosine triphosphate, and nucleotides are just a few examples that are available in caged form [55]. In time-resolved crystallography, caged substrates are soaked into crystals and then activated using a light pulse with some notable examples. Caged guanosine triphosphate was successfully used to study Ras P21 [56], the reaction catalyzed by isocitrate dehydrogenase was investigated using caged nicotinamide adenine dinucleotide phosphate [57], and acetylcholinesterase was examined with caged choline [11]. However, wide spread use of caged compounds in time-resolved crystallography is challenging due to several factors: (1) the design and fabrication of caged substrates requires significant expertise, (2) each substrate is specifically tailored to the protein and the reaction to be investigated, (3) the photo-removable protecting groups need to meet high specifications such as high quantum yield of the photoreaction, and high absorbance above the 300 nm wavelength to limit protein photo-damage [55], (4) once the protecting group has been removed, the byproducts should not harm the protein nor inhibit the reaction with the substrate, (5) activation must occur on a faster time-scale than the reaction being probed (Table 12.1), and

(6) cleavage of the protecting group induced by X-ray exposure must be kept to a minimum when longer or multiple X-ray pulses are required. All of these largely impede the routine application to time-resolved crystallographic investigations.

12.2.3 Other Activation Mechanisms

By recombinantly attaching a light activated domain to an enzyme its activity can be controlled by light [58, 59]. The time delay between light activation and signal transmission to the effector domain is in the range of microseconds, which allows the observation of enzymatic processes that occur on the millisecond time-scale [60]. Recently, a reaction has been triggered by an electric field [41], which would alter charges, dipoles, and polarizability. This will affect any movement of charge within a protein, and therefore is a general method to study structural dynamics. However, it is not clear how the vast number of very specific enzymatic reactions can be triggered by this method.

12.2.4 Activation by Diffusion

A versatile option to initiate a reaction for non-photosensitive proteins is through diffusion. The crystals are simply mixed with substrate such as small molecules, redox reagents, or other cofactors. Although this is conceptually a simple method, in practice diffusive studies with crystals are difficult because diffusion is an inherently slow process. Depending on crystal size, protein packing density in the crystal, size of the substrate, and the type of chemicals that are used for crystallization, the substrate can take seconds to even minutes to diffuse throughout the crystal [61–64].

For previous diffusion-based work at synchrotrons, flow cells were used to collect data [65–67]. A flow cell works by immobilizing a crystal inside of a capillary while flowing a solution with the substrate over the crystal [67]. This approach has been successfully used to determine the structure of rate-limited species that accumulate enough in the steady state [10]. Common challenges when working with flow cells are crystal mounting, keeping the crystal centered, and keeping it immobilized in the X-ray beam even as the substrate solution is flowing [6, 68]. On the other hand, serial femtosecond crystallography seems to be almost tailor made for a diffusion-based method, as microcrystals allow for rapid diffusion. Microcrystals mixed with substrate can be utilized at high-intensity X-ray FEL sources, or with micro-focused pulsed X-ray beams from synchrotrons, using a technique called "mix-and-inject serial crystallography" (MISC) [40]. MISC works through rapid diffusion of a substrate into a slurry of microcrystals or nanocrystals just prior to the X-ray interaction region [69]. The method to accomplish this is discussed below. With sizes approximately 10 μm or less, microcrystals allow millisecond or even sub-millisecond diffusion times [69] with estimated diffusion times for several

Table 12.2 Diffusion times into crystals as determined by calculation, simulation and experiment

Crystal size (μm^3)	$0.5 \times 0.5 \times 0.5$	$1 \times 2 \times 3$	$3 \times 4 \times 5$	$10 \times 20 \times 30$	$400 \times 400 \times 1600$
Diffusion time	17 μs[a]	150 μs[a]	1 ms[a]	15 ms[a]	16 s[a]24 s[b]<1 min[c]

[a]Times from [69]
[b]Time from [61]
[c]Time from [62]

crystal sizes shown in Table 12.2. Fortunately, very fast enzyme catalysis is still in the range of tens of microseconds [70], while most enzymatic reactions occur in the millisecond time regime.

12.3 Sample Delivery

In synchrotron-based crystallography a single large crystal can be used to collect multiple data sets [22, 24–26] or even a complete time-series [16, 19, 21]. In most room temperature synchrotron experiments, crystals are individually mounted and sealed in a capillary with a small amount of mother liquor to prevent them from drying out. This is very different from serial crystallography, in which tens of thousands of microcrystals are introduced into the X-ray interaction region one at a time in random orientation. Serial crystallography can be performed at X-ray FELs and at synchrotrons. At synchrotrons, somewhat large crystals (>10 μm) are needed, which ameliorate radiation damage and scatter with higher intensities. The velocity at which the crystals move through the X-ray interaction volume needs to be adjusted so that there is negligible crystal motion during the longer (100 ps) synchrotron pulse. In the case of X-ray FELs, crystals sizes can be smaller, allowing for more rapid diffusion and all crystal displacements are negligible during the femtosecond X-ray pulses. In recent years, numerous microcrystalline injection methods have been developed. Depending on factors like time scale and sample consumption, sample delivery systems such as the gas dynamics virtual nozzle [71], viscous jet [72, 73], electrospun jet [74, 75], fixed target system [76–79], and the droplet on demand system [80] are all viable options. These systems are compatible with time-resolved studies triggered by light, however none of these were designed for introducing small molecules for mixing. Therefore for mix-and-inject experiments special injectors had to be developed such as the one shown in Fig. 12.2. Mixing times must be as quick as possible, and diffusion times fast to allow for sufficient time-resolution. The time delay is given by the difference in distance between the mixing region and the X-ray interaction volume divided by the jet velocity. New generations of injector technology allows for the rapid mixing of substrate with enzyme in crystal form [39, 40]. Current capabilities support mixing times on the microsecond to millisecond time scales, significantly faster than the majority of enzymatic reactions. If longer time scales are of interest, a simple T-junction mixer can also be used, as shown in Fig. 12.3.

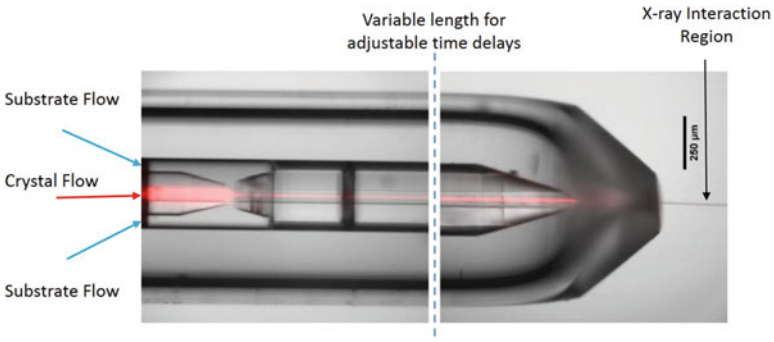

Fig. 12.2 Mixing injector, picture modified from Calvey et al., Structural Dynamics, 3, 054301, 2016. Crystal suspension, simulated by central red flow, is focused by the substrate flow, blue arrows. The mixture is then gas focused to produce a jet to be probed by the X-ray FEL pulse. The time delay is variable depending on the distance between the mixing region and the X-ray interaction region. This allows for the collection of multiple time points [39]

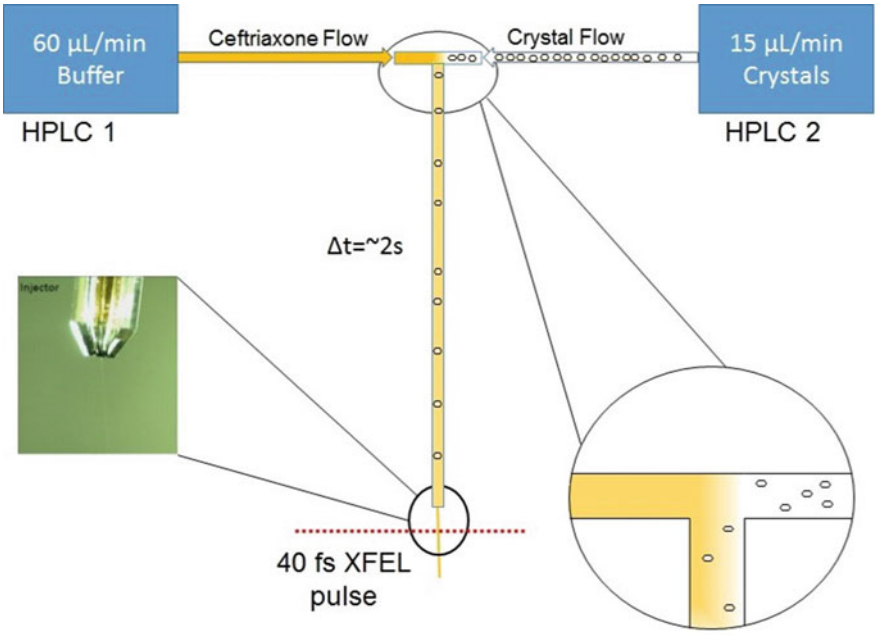

Fig. 12.3 Schematic example of the T-junction mixer used at LCLS for mix-and-inject serial crystallography. Substrate is pumped by HPLC 1, crystals are pumped by HPLC 2. The distance from the mixer to the X-ray interaction zone along with the velocity of crystal flow determines the time-delay. In this setup, the crystals are injected into the X-ray interaction region via a standard gas dynamic virtual nozzle

12.4 Data Analysis of Serial and Time-Resolved Crystallography

Data analysis of X-ray FEL data has come a long way since the first days of X-ray FEL based crystallography. All the standard methods for hit finding and Bragg intensity integration developed for SFX apply to time-resolved SFX as well. It is a simple matter of properly tagging which shots are "delayed" after the initiation of a reaction in the crystals, and what the delay times are for each X-ray exposure. Separate data sets of structure factor amplitudes for each time delay (including the reference with $t = 0$) are then available. Details on SFX data analysis can be found in Chap. 7 of this book. An overview of the entire data analysis process is shown in Fig. 12.4.

12.4.1 Difference Maps

A time-series of difference electron density maps lies at the core of time-resolved crystallography. If the unit cell does not change during the reaction, isomorphous difference maps can be calculated from reference amplitudes collected without reaction initiation ($|F_r|$) and the time-dependent amplitudes ($|F_t|$) collected some time interval (t) after reaction initiation. Phases (ϕ^{calc}) are obtained from an accurate reference model. Difference amplitudes are calculated by subtracting the F_t^{obs} from the F_r^{obs}: $\Delta F_t = |F_t^{\text{obs}}| - |F_r^{\text{obs}}|$. ΔF_t can be weighted [32, 49, 81] in order to account for errors in the measured amplitudes that might impair the proper interpretation of the maps. The weighting factor ensures that those difference structure factor amplitudes, which are erroneously large or contain large experimental error values, are down-weighted appropriately. An example of a difference map is shown in Fig. 12.4.

If unit cell parameters largely change [30], or even the space group changes [82] during a reaction, the reference and the time-dependent crystallographic data are

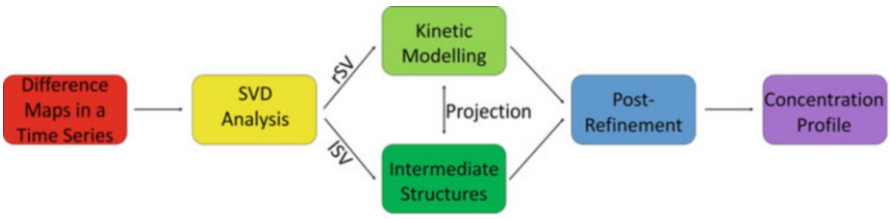

Fig. 12.4 SVD-based analysis of experimental difference maps allows the determination of the structures of the intermediates by applying a kinetic model. The kinetic mechanism is further post-refined (see text). As a result the concentrations of the intermediates at all time points (the concentration profile) can be determined

no longer isomorphous. Difference maps cannot be calculated by subtracting the observed reference data. In this case omit maps, preferentially generated using a simulated annealing (SA) refinement strategy, can circumvent this problem. Before the refinement, parts of the model where changes are expected are deliberately removed. Then this structural model is heated in the computer to several thousand Kelvin, gradually cooled and simultaneously refined against the time-resolved structure factor amplitudes [83, 84]. This strategy eliminates model phase bias which would otherwise impair the reliability of the difference map [84]. After the refinement, structure factors F^{calc} with amplitude $|F^{\text{calc}}|$ and phase ϕ^{omit} can be determined. Maps calculated with $\Delta F_t{}^{\text{omit}} = |F_t{}^{\text{obs}}|\text{-}|F^{\text{calc}}|$ and model phases ϕ^{omit} show unbiased difference electron density, which accounts for the local structural changes during a reaction. This SA omit map can then be structurally explained either by reinterpreting the missing part that was omitted in the refinement, or by adding ligands that coordinate during the reaction, or both. Either way, omit maps (when there is non-isomorphism) or isomorphous difference maps are equally suitable to extract the kinetics.

The methods discussed above in conjunction with high-resolution time-resolved serial femtosecond crystallographic experiment at the LCLS were demonstrated to be highly successful. Difference maps were generated that contain features with high signal to noise ratio and show chemically sensible structural changes of PYP [32]. An example of the difference maps generated for PYP can be seen in Fig. 12.4. Here the difference density clearly shows changes between the reference model (PG, yellow) and the pR_2 model (red) and pR_1 model (magenta), with the negative features of the electron density map primarily on top of the atoms of the reference model. These structures are part of the photocycle as shown in Fig. 12.4a.

12.4.2 Kinetic Mechanism and Intermediates and Detangling Multiple States

Chemical kinetics is governed by a kinetic mechanism with one or more intermediate states connected by rate coefficients (see above). Intermediate states are occupied (or visited) by macromolecules whose concentrations then vary as a function of time. This means multiple states may be occupied at the same time (see Fig. 12.5 for an example). Thus, a time-resolved experiment will probe this mixture of states. As mentioned earlier, a way to separate this mixture into its components is required. The singular value decomposition (SVD) method has been successfully used for this purpose [16, 18, 32, 85]. The SVD method separates out the spatial and temporal dependencies in the time-series of difference maps [18]. Two sets of vectors are obtained, the left singular vector (lSV) and the right singular vector (rSV). The lSV contains the spatial components, which are difference maps, while the rSVs contain the corresponding time evolutions. The significant rSVs are then interpreted with a kinetic model. This requires a kinetic mechanism with a corresponding set of coupled differential equations that contain rate coefficients [18]. A compatible

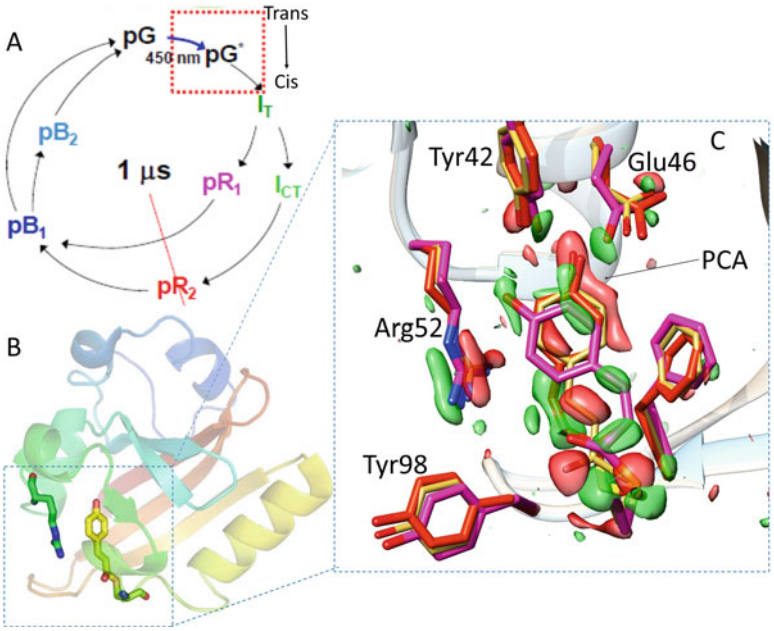

Fig. 12.5 Photoactive yellow protein (PYP). (**a**) Overview of the PYP photocycle. The reaction can be triggered by 450 nm light. I_T is an early intermediate already in the cis configuration. pR_1 is an intermediate also identified by spectroscopy. Its absorption maximum is red-shifted. I_{CT} is slightly changed from I_T. pR_2 is the second red-shifted intermediate. The red box denotes a part of the photo cycle that is faster than the time-resolution of synchrotrons. The red line denotes the 1 µs time point that is observed in (**c**). (**b**) An overview of PYP structure. (**c**) An isomorphous difference map of the chromophore pocket of PYP calculated from a 1 µs time delay data set collected at the LCLS. Green denotes positive difference density, red denotes negative difference density, both are contoured to 3σ and −3σ respectively. The structures of pR_1, pR_2, and pG (reference) are shown in magenta, red and yellow respectively. The chromophore has undergone photo isomerization from trans to cis. Several nearby residues have changed their conformation

mechanism must match the observed relaxation times in the rSV. Globally fitting sums of exponentials to the significant rSVs provides this number of relaxation times. The number of significant right singular vectors, significant singular values, and the exponentials should all be compatible with the number of distinguishable intermediates. After fitting the right singular vectors with concentration profiles of a compatible chemical kinetic mechanism, time-independent difference maps can then be calculated for each intermediate state using a projection algorithm [18, 86].

12.4.3 Structures of the Intermediate

Once the mixture-free, time-independent difference electron densities of the intermediates have been extracted, the structures of the intermediates can be determined.

A convenient way is to use extrapolated, conventional electron density maps for this purpose. To calculate these maps, difference structure factors ΔF_j^{ind} for all intermediates, $j = 1 \ldots J$ are determined by Fourier transforming the time-independent difference maps. A multiple, N, of these difference structure factors need to be added to the calculated structure factors F_r^{calc} derived from a reference model.

Extrapolated maps for all the intermediates, ρ_j^{ext}, are calculated from the F_j^{ext}. The multiplier N must be optimized so that the electron density in a particular extrapolated map vanishes where negative electron density is present in the corresponding difference map. Extrapolated maps can be interpreted just like conventional electron density maps. Since structural changes are usually small, most of the electron density in the extrapolated map can be explained already by the reference model. This will also allow for a direct structural refinement. In areas where there is a strong deviation between the reference model and the electron density, a program like "Coot" [87] is used to adjust the model by hand to better match the electron density. The resulting model can be refined in real space against the electron density before performing the final refinement in reciprocal space using the $|F_j^{\text{ext}}|$ with standard programs such as "Refmac" [88] or "Phenix" [83].

12.4.4 Post-Analysis

The purpose of this analysis is to refine a candidate kinetic mechanism by making use of the experimentally determined intermediate structures. Calculated time-dependent difference maps ($\Delta\rho(t)^{\text{calc}}$) must agree with the observed time-dependent difference maps ($\Delta\rho(t)^{\text{obs}}$). In order to obtain the $\Delta\rho(t)^{\text{calc}}$, several steps are required. (1) Structure factors for each of the J intermediates are computed from their respective structural models. From these, time-independent difference structure factors, ΔF_j^{calc}, can be determined by subtracting the structure factors of the reference model. (2) The ΔF_j^{calc} are used to determine time-independent difference electron density maps ($\Delta\rho_j^{\text{calc}}$). (3) Time-dependent concentrations, $c(t,k)_j$, for each intermediate are calculated by integrating the coupled differential equations of the candidate kinetic mechanism [18]. Note that $c(t,k)$ is determined by the magnitude of the rate coefficients of the mechanism. Finally, (4) $\Delta\rho(t)^{\text{calc}}$ is calculated by adding together individual time-independent difference electron density maps $\Delta\rho_j^{\text{calc}}$, which are weighted by their time-dependent concentrations $c(t)_j$ at all time-points.

The time-series of $\Delta\rho(t)^{\text{calc}}$ can then be compared to the observed $\Delta\rho(t)^{\text{obs}}$. The $\Delta\rho(t)^{\text{calc}}$ are dependent on both the rate coefficients and a global scaling factor (sc). The sc accounts for the difference in scale between the observed and calculated difference electron densities. The rate coefficients and the scale factor are iteratively changed to optimize the agreement between the difference density maps at all time-points. The final result of this analysis is a series of refined rate coefficients, which can be used to determine a refined concentration profile (Fig. 12.1b) for all

intermediates. The scale factor is a measure for the extent of reaction initiation. It accounts for the number of molecules that enter the reaction in the crystal. In some cases the extent of the reaction initiation is small, only around 5–10%, however activation yields as high as 40–50% have been reported [21, 25, 32].

12.5 Results of Mix-and-Inject Serial Crystallography

Results using MISC have recently been reported [40, 82], in which a T-junction (Fig. 12.3) was used to mix substrate and microcrystals. In one study, an overall reaction time of 2 s [40] was selected, and in the other reaction times of 10 s as well as 10 min were reported [82]. These results are summarized below.

Successful experiments on a ß-lactamase (BlaC) mixed with the third generation lactam antibiotic Ceftriaxone were published by Kupitz et al. [40]. BlaC from *M. tuberculosis* is responsible for broad resistance of the bacteria to lactam antibiotics, such as penicillin and cephalosporin derivatives [89, 90]. BlaC microcrystals were grown via ammonium phosphate in thin plates, and then crushed using glass beads to small shards. These shards, which contain ~16 mmol/L of BlaC, were mixed with 200 mmol/L ceftriaxone. The crystal-substrate suspension was probed by an X-ray FEL pulse approximately 2 s after mixing (Fig. 12.3). The results from this experiment were maps generated at approximately 2.4 Å resolution. The electron density was found to have changed in the catalytic cleft of BlaC in two out of four subunits of the asymmetric unit (Fig. 12.6).

Since the turnover time of Ceftriaxone is 1.2 s [91], most likely a steady state was observed. In the steady state, three states can contribute to the electron density. The enzyme-substrate complex (ES) in which the full ceftriaxone molecule is intact prior to any attack by Ser70 is the first contributor. The second contributor is the covalently bound serine-adduct in which ceftriaxone is bound to Ser70. The lactam ring is cleaved opened, and a portion of the ceftriaxone molecule has been cleaved off [92]. It might also be that the third contributor is the product form in which the ceftriaxone molecule is hydrolyzed from Ser70 after the lactam ring has been opened. The full length model of ceftriaxone fits the electron density best, although the two other models both might provide slight perturbations, which improve the fit to the electron density. Moreover it is both interesting and important to note that the electron density reported here only shows ceftriaxone in two (subunits B and D) of the four subunits present in the asymmetric unit. Not all subunits may react equally, depending on accessibility of the binding pocket and its chemical environment. In addition, crystal lattice constraints might influence the dynamics of the enzyme molecules. Therefore, reaction rates may be different in the crystal compared to those in solution.

MISC has also been used to determine structures during the binding of adenine to a RNA-riboswitch [82] at 10 s and approximately 10 min. For the 10 s time point, the injection method was similar to the double HPLC T-junction setup shown

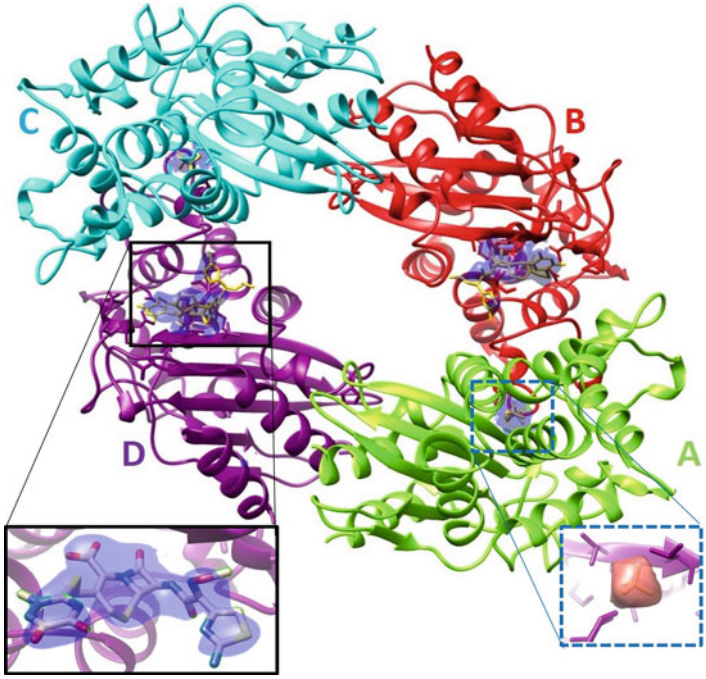

Fig. 12.6 BlaC tetramer after 2 s mixing with ceftriaxone, subunits (**a**–**d**) labelled. (**b**) and (**d**) subunits show ceftriaxone electron density (blue density inside solid black box), (**a**) and (**c**) subunits show only phosphate density (red density inside blue dashed box). The catalytic clefts of subunits (**a**) and (**c**) are blocked from interaction by the neighboring subunits

in Fig. 12.3. For the 10 min time point substrate was directly added to crystals and allowed to react before injection. During this time, unit cell parameters changed. For example, the length of cell parameter b increased from 46.7 to 154.9 Å. Even the crystallographic space group changed from $P2_1$ to $P2_12_12$. Remarkably, the crystals accommodated these large changes, and still diffracted to 3.0 Å.

As discussed above, mixtures can only be separated when a time-series with shortly space time-points is used. The ability to collect X-ray data at various time-delays is a major goal at X-ray FEL facilities. Enzymatic intermediates along a catalytic pathway can then be extracted. The mix-and-inject method, when applied to medically or pharmaceutically important targets, will become an integral tool in the field of structural based drug design. The above examples demonstrate that it is necessary to collect full time-series on catalytically active targets routinely. With continued effort in injector technology [39, 93] to decrease mixing times, the time resolution can be improved, and faster reactions can be visualized on the sub-millisecond time scale.

12.6 Moving Forward

Time-resolved crystallography is currently entering a new era. Previously, time-resolved crystallography was mostly limited to light-activated reversible reactions, such as those observed in PYP [17, 19, 27, 81] or in various heme proteins [22, 25, 26, 43]. Most biological, pharmaceutical and medical important reactions have not been explored.

The advent of the X-ray FEL allows the use of microscopic crystals. This provides new opportunities to investigate enzymes. Several studies have already been reported that have successfully used diffusion-based techniques at an X-ray FEL to explore structural changes on the second time scale. Continuing work on injector technology promises mix-and-inject delivery with time resolution as fast as microseconds [39]. Through the use of slightly larger micron sized crystals, mix-and-inject experiments can also be performed at synchrotrons. A 5 μm crystal still allows for an achievable time resolution of better than 10 ms, which is sufficient for most enzymatic reactions, while still tolerating the radiation dose deposited by the synchrotron pulses [94]. Beamtimes at XFELs are limited. Synchrotron light sources may provide additional beamtime for these investigations, so that more biologically and biomedically important biomolecules can be examined this way.

With all of these new techniques and sources on the horizon, the future of structural biology and specifically structural enzymology is bright. Moving forward, the goals of crystallographers will change from the determination of static images and stills of protein molecules to the collection of comprehensive time-courses. From one well-planned, essentially routine experiment not only the three-dimensional structure of the biological macromolecule can be solved, but also its function, kinetics, and dynamics may be extracted.

From one well-planned, essentially routine experiment not only the three-dimensional structure of the biological macromolecule can be solved, but also it's function, kinetics, and dynamics may be extracted, as most recently demonstrated by Olmos et al, 2018

References

1. DePristo, M. A., de Bakker, P. I., & Blundell, T. L. (2004). Heterogeneity and inaccuracy in protein structures solved by X-ray crystallography. *Structure, 12*, 831–838.
2. Botha, S., Nass, K., Barends, T. R., Kabsch, W., Latz, B., Dworkowski, F., et al. (2015). Room-temperature serial crystallography at synchrotron X-ray sources using slowly flowing free-standing high-viscosity microstreams. *Acta Crystallographica. Section D, Biological Crystallography, 71*, 387–397.
3. Frauenfelder, H., Sligar, S. G., & Wolynes, P. G. (1991). The energy landscapes and motions of proteins. *Science, 254*, 1598–1603.
4. McCammon, J. A., & Harvey, S. C. (1987). *Dynamics of proteins and nucleic acids*. Cambridge, UK: Cambridge University Press.

5. Steinbach, P. J., Ansari, A., Berendzen, J., Braunstein, D., Chu, K., Cowen, B. R., et al. (1991). Ligand binding to heme proteins: Connection between dynamics and function. *Biochemistry, 30*, 3988–4001.
6. Moffat, K. (1989). Time-resolved macromolecular crystallography. *Annual Review of Biophysics and Biophysical Chemistry, 18*, 309–332.
7. Moffat, K. (2001). Time-resolved biochemical crystallography: A mechanistic perspective. *Chemical Reviews, 101*, 1569–1581.
8. Schmidt, M. (2008). Structure based enzyme kinetics by time-resolved X-ray crystallography. In *Ultrashort laser pulses in medicine and biology*. Berlin, Germany: Springer.
9. Schmidt, M. (2015). Time-resolved crystallography at X-ray free Electron lasers and synchrotron light sources. *Synchrotron Radiation News, 28*, 25–30.
10. Stoddard, B. L. (2001). Trapping reaction intermediates in macromolecular crystals for structural analyses. *Methods, 24*, 125–138.
11. Bourgeois, D., & Weik, M. (2009). Kinetic protein crystallography: A tool to watch proteins in action. *Crystallography Reviews, 15*, 87–118.
12. Flint, A. J., Tiganis, T., Barford, D., & Tonks, N. K. (1997). Development of "substrate-trapping" mutants to identify physiological substrates of protein tyrosine phosphatases. *Proceedings of the National Academy of Sciences of the United States of America, 94*, 1680–1685.
13. Buch, I., Giorgino, T., & De Fabritiis, G. (2011). Complete reconstruction of an enzyme-inhibitor binding process by molecular dynamics simulations. *Proceedings of the National Academy of Sciences of the United States of America, 108*, 10184–10189.
14. Schmidt, M., & Saldin, D. K. (2014). Enzyme transient state kinetics in crystal and solution from the perspective of a time-resolved crystallographer. *Structural Dynamics, 1*, 1–14.
15. Steinfeld, J. I., Francisco, J. S., & Hase, W. L. (1985). *Chemical kinetics and dynamics*. Upper Saddle River, NJ: Prentience Hall.
16. Schmidt, M., Srajer, V., Henning, R., Ihee, H., Purwar, N., Tenboer, J., et al. (2013). Protein energy landscapes determined by five-dimensional crystallography. *Acta Crystallographica Section D, 69*, 2534–2542.
17. Rajagopal, S., Anderson, S., Srajer, V., Schmidt, M., Pahl, R., & Moffat, K. (2005). A structural pathway for signaling in the E46Q mutant of photoactive yellow protein. *Structure, 13*, 55–63.
18. Schmidt, M., Rajagopal, S., Ren, Z., & Moffat, K. (2003). Application of singular value decomposition to the analysis of time-resolved macromolecular X-ray data. *Biophysical Journal, 84*, 2112–2129.
19. Ihee, H., Rajagopal, S., Srajer, V., Pahl, R., Anderson, S., Schmidt, M., et al. (2005). Visualizing reaction pathways in photoactive yellow protein from nanoseconds to seconds. *Proceedings of the National Academy of Sciences of the United States of America, 102*, 7145–7150.
20. Jung, Y. O., Lee, J. H., Kim, J., Schmidt, M., Moffat, K., Srajer, V., et al. (2013). Volume-conserving trans-cis isomerization pathways in photoactive yellow protein visualized by picosecond X-ray crystallography. *Nature Chemistry, 5*, 212–220.
21. Knapp, J. E., Pahl, R., Srajer, V., & Royer, W. E., Jr. (2006). Allosteric action in real time: Time-resolved crystallographic studies of a cooperative dimeric hemoglobin. *Proceedings of the National Academy of Sciences of the United States of America, 103*, 7649–7654.
22. Schmidt, M., Nienhaus, K., Pahl, R., Krasselt, A., Anderson, S., Parak, F., et al. (2005). Ligand migration pathway and protein dynamics in myoglobin: A time-resolved crystallographic study on L29W MbCO. *Proceedings of the National Academy of Sciences of the United States of America, 102*, 11704–11709.
23. Schotte, F., Cho, H. S., Kaila, V. R., Kamikubo, H., Dashdorj, N., Henry, E. R., et al. (2012). Watching a signaling protein function in real time via 100-ps time-resolved Laue crystallography. *Proceedings of the National Academy of Sciences of the United States of America, 109*, 19256–19261.
24. Schotte, F., Lim, M., Jackson, T. A., Smirnov, A. V., Soman, J., Olson, J. S., et al. (2003). Watching a protein as it functions with 150-ps time-resolved X-ray crystallography. *Science, 300*, 1944–1947.

25. Srajer, V., Ren, Z., Teng, T. Y., Schmidt, M., Ursby, T., Bourgeois, D., et al. (2001). Protein conformational relaxation and ligand migration in myoglobin: A nanosecond to millisecond molecular movie from time-resolved Laue X-ray diffraction. *Biochemistry, 40*, 13802–13815.
26. Srajer, V., Teng, T. Y., Ursby, T., Pradervand, C., Ren, Z., Adachi, S., et al. (1996). Photolysis of the carbon monoxide complex of myoglobin: Nanosecond time-resolved crystallography. *Science, 274*, 1726–1729.
27. Tripathi, S., Srajer, V., Purwar, N., Henning, R., & Schmidt, M. (2012). pH dependence of the photoactive yellow protein photocycle investigated by time-resolved crystallography. *Biophysical Journal, 102*, 325–332.
28. Boutet, S., Lomb, L., Williams, G. J., Barends, T. R., Aquila, A., Doak, R. B., et al. (2012). High-resolution protein structure determination by serial femtosecond crystallography. *Science, 337*(6092), 362–364.
29. Chapman, H. N., Fromme, P., Barty, A., White, T. A., Kirian, R. A., Aquila, A., et al. (2011). Femtosecond X-ray protein nanocrystallography. *Nature, 470*, 73–77.
30. Kupitz, C., Basu, S., Grotjohann, I., Fromme, R., Zatsepin, N. A., Rendek, K. N., et al. (2014). Serial time-resolved crystallography of photosystem II using a femtosecond X-ray laser. *Nature, 513*, 5.
31. Pande, K., Hutchison, C. D. M., Groenhof, G., Aquila, A., Robinson, J. S., Tenboer, J., et al. (2016). Femtosecond structural dynamics drives the trans/Cis isomerization in photoactive yellow protein. *Science, 352*, 725–729.
32. Tenboer, J., Basu, S., Zatsepin, N., Pande, K., Milathianaki, D., Frank, M., et al. (2014). Time-resolved serial crystallography captures high-resolution intermediates of photoactive yellow protein. *Science, 346*, 1242–1246.
33. Neutze, R., Wouts, R., van der Spoel, D., Weckert, E., & Hajdu, J. (2000). Potential for biomolecular imaging with femtosecond X-ray pulses. *Nature, 406*, 752–757.
34. Chapman, H. N., Barty, A., Bogan, M. J., Boutet, S., Frank, M., Hau-Riege, S. P., et al. (2006). Femtosecond diffractive imaging with a soft-X-ray free-electron laser. *Nature Physics, 2*, 839–843.
35. Aquila, A., Hunter, M. S., Doak, R. B., Kirian, R. A., Fromme, P., White, T. A., et al. (2012). Time-resolved protein nanocrystallography using an X-ray free-electron laser. *Optics Express, 20*, 2706–2716.
36. Barty, A., Caleman, C., Aquila, A., Timneanu, N., Lomb, L., White, T. A., et al. (2012). Self-terminating diffraction gates femtosecond X-ray nanocrystallography measurements. *Nature Photonics, 6*, 35–40.
37. Parak, F. G., Achterhold, K., Croci, S., & Schmidt, M. (2007). A physical picture of protein dynamics and conformational changes. *Journal of Biological Physics, 33*, 371–387.
38. Bourgeois, D., & Weik, M. (2005). *New perspectives in kinetic protein crystallography using caged compounds*. Hoboken, NJ: Wiley.
39. Calvey, G. D., Katz, A. M., Schaffer, C. B., & Pollack, L. (2016). Mixing injector enables time-resolved crystallography with high hit rate at X-ray free electron lasers. *Structural Dynamics, 3*, 054301.
40. Kupitz, C., Olmos, J., Holl, M., Tremblay, L. W., Pande, K., Pandey, S., et al. (2017). Structural enzymology using X-ray free Electron lasers. *Structural Dynamics, 4*, 044003.
41. Hekstra, D. R., White, K. I., Socolich, M. A., Henning, R. W., Srajer, V., & Ranganathan, R. (2016). Electric-field-stimulated protein mechanics. *Nature, 540*, 400–405.
42. Spence, J. C., Weierstall, U., & Chapman, H. N. (2012). X-ray lasers for structural and dynamic biology. Reports on progress in physics. *Physical Society, 75*, 102601.
43. Key, J. M., Srajer, V., Pahl, R., & Moffat, K. (2004). Time-resolved crystallographic studies of the heme-based sensor protein FixL. *Biophysical Journal, 86*, 246a–246a.
44. Barends, T. R., Foucar, L., Ardevol, A., Nass, K., Aquila, A., Botha, S., et al. (2015). Direct observation of ultrafast collective motions in CO myoglobin upon ligand dissociation. *Science, 350*(6259), 445–450.

45. Barty, A., Kirian, R. A., Maia, F. R. N. C., Hantke, M., Yoon, C. H., White, T. A., et al. (2014). Cheetah: Software for high-throughput reduction and analysis of serial femtosecond X-ray diffraction data. *Journal of Applied Crystallography, 47*, 1118–1131.
46. Bourgeois, D., Vallone, B., Arcovito, A., Sciara, G., Schotte, F., Anfinrud, P. A., et al. (2006). Extended subnanosecond structural dynamics of myoglobin revealed by Laue crystallography. *Proceedings of the National Academy of Sciences of the United States of America, 103*, 4924–4929.
47. Nienhaus, K., Ostermann, A., Nienhaus, G. U., Parak, F. G., & Schmidt, M. (2005). Ligand migration and protein fluctuations in myoglobin mutant L29W. *Biochemistry, 44*, 5095–5105.
48. Schmidt, M., Graber, T., Henning, R., & Srajer, V. (2010). Five-dimensional crystallography. *Acta crystallographica. Section A, Foundations of crystallography, 66*, 198–206.
49. Schmidt, M., Ihee, H., Pahl, R., & Srajer, V. (2005). Protein-ligand interaction probed by time-resolved crystallography. *Methods in Molecular Biology, 305*, 115–154.
50. Van Brederode, M. E., Hoff, W. D., Van Stokkum, I. H., Groot, M. L., & Hellingwerf, K. J. (1996). Protein folding thermodynamics applied to the photocycle of the photoactive yellow protein. *Biophysical Journal, 71*, 365–380.
51. Hutchison, C. D. M., Tenboer, J., Kupitz, C., Moffat, K., Schmidt, M., & van Thor, J. J. (2016). Photocycle populations with femtosecond excitation of crystalline photoactive yellow protein. *Chemical Physics Letters, 654*, 63–71.
52. Lincoln, C. N., Fitzpatrick, A. E., & van Thor, J. J. (2012). Photoisomerisation quantum yield and non-linear cross-sections with femtosecond excitation of the photoactive yellow protein. *Physical Chemistry Chemical Physics: PCCP, 14*, 15752–15764.
53. Bourgeois, D., & Royant, A. (2005). Advances in kinetic protein crystallography. *Current Opinion in Structural Biology, 15*, 538–547.
54. Pelliccioli, A. P., & Wirz, J. (2002). Photoremovable protecting groups: Reaction mechanisms and applications. *Photochemical & Photobiological Sciences, 1*, 441–458.
55. Goelder, M., & Givens, R. (2005). *Dynamic studies in biology: Phototriggers, photoswitches and caged biomolecules*. Hoboken, NJ: Wiley.
56. Schlichting, I., Almo, S. C., Rapp, G., Wilson, K., Petratos, K., Lentfer, A., et al. (1990). Time-resolved X-ray crystallographic study of the conformational change in ha-Ras P21 protein on Gtp hydrolysis. *Nature, 345*, 309–315.
57. Stoddard, B. L., Cohen, B. E., Brubaker, M., Mesecar, A. D., & Koshland, D. E., Jr. (1998). Millisecond Laue structures of an enzyme-product complex using photocaged substrate analogs. *Nature Structural Biology, 5*, 891–897.
58. Moglich, A., & Hegemann, P. (2013). Biotechnology: Programming genomes with light. *Nature, 500*, 406–408.
59. Moglich, A., & Moffat, K. (2010). Engineered photoreceptors as novel optogenetic tools. *Photochemical & Photobiological Sciences, 9*, 1286–1300.
60. Crosson, S., & Moffat, K. (2002). Photoexcited structure of a plant photoreceptor domain reveals a light-driven molecular switch. *The Plant Cell, 14*, 1067–1075.
61. Geremia, S., Campagnolo, M., Demitri, N., & Johnson, L. N. (2006). Simulation of diffusion time of small molecules in protein crystals. *Structure, 14*, 393–400.
62. Hajdu, J., Acharya, K. R., Stuart, D. I., Mclaughlin, P. J., Barford, D., Oikonomakos, N. G., et al. (1987). Catalysis in the crystal - synchrotron radiation studies with glycogen phosphorylase-B. *The EMBO Journal, 6*, 539–546.
63. Sjogren, T., Svensson-Ek, M., Hajdu, J., & Brzezinski, P. (2000). Proton-coupled structural changes upon binding of carbon monoxide to cytochrome cd1: A combined flash photolysis and X-ray crystallography study. *Biochemistry, 39*, 10967–10974.
64. Sluyterman, L. A., & de Graaf, M. J. (1969). The activity of papain in the crystalline state. *Biochimica et Biophysica Acta, 171*, 277–287.
65. Kim, T. H., Mehrabi, P., Ren, Z., Sljoka, A., Ing, C., Bezginov, A., et al. (2017). The role of dimer asymmetry and protomer dynamics in enzyme catalysis. *Science, 355*, 28104837.
66. Kurisu, G., Sugimoto, A., Kai, Y., & Harada, S. (1997). A flow cell suitable for time-resolved X-ray crystallography by the Laue method. *Journal of Applied Crystallography, 30*, 555–556.

67. Petsko, G. A. (1985). Diffraction methods for biological macromolecules. Flow cell construction and use. *Methods in Enzymology, 114*, 141–146.
68. Chupas, P. J., Chapman, K. W., Kurtz, C., Hanson, J. C., Lee, P. L., & Grey, C. P. (2008). A versatile sample-environment cell for non-ambient X-ray scattering experiments. *Journal of Applied Crystallography, 41*, 822–824.
69. Schmidt, M. (2013). Mix and inject, reaction initiation by diffusion for time-resolved macromolecular crystallography. *Advances on Condensed Matter Physics, 2013*, 1–10.
70. Purwar, N., McGarry, J. M., Kostera, J., Pacheco, A. A., & Schmidt, M. (2011). Interaction of nitric oxide with catalase: Structural and kinetic analysis. *Biochemistry, 50*, 4491–4503.
71. Weierstall, U., Spence, J. C., & Doak, R. B. (2012). Injector for scattering measurements on fully solvated biospecies. *The Review of Scientific Instruments, 83*, 035108.
72. Nogly, P., James, D., Wang, D., White, T. A., Zatsepin, N., Shilova, A., et al. (2015). Lipidic cubic phase serial millisecond crystallography using synchrotron radiation. *IUCrJ, 2*, 168–176.
73. Weierstall, U., James, D., Wang, C., White, T. A., Wang, D., Liu, W., et al. (2014). Lipidic cubic phase injector facilitates membrane protein serial femtosecond crystallography. *Nature Communications, 5*, 3309.
74. Sierra, R. G., Gati, C., Laksmono, H., Dao, E. H., Gul, S., Fuller, F., et al. (2016). Concentric-flow electrokinetic injector enables serial crystallography of ribosome and photosystem II. *Nature Methods, 13*, 59–62.
75. Sierra, R. G., Laksmono, H., Kern, J., Tran, R., Hattne, J., Alonso-Mori, R., et al. (2012). Nanoflow electrospinning serial femtosecond crystallography. *Acta Crystallographica. Section D, Biological Crystallography, 68*, 1584–1587.
76. Hunter, M. S., Segelke, B., Messerschmidt, M., Williams, G. J., Zatsepin, N. A., Barty, A., et al. (2014). Fixed-target protein serial microcrystallography with an X-ray free electron laser. *Scientific Reports, 4*, 6026.
77. Mueller, C., Marx, A., Epp, S. W., Zhong, Y., Kuo, A., Balo, A. R., et al. (2015). Fixed target matrix for femtosecond time-resolved and in situ serial micro-crystallography. *Structural Dynamics, 2*(5), 054302.
78. Perry, S. L., Guha, S., Pawate, A. S., Henning, R., Kosheleva, I., Srajer, V., et al. (2014). In situ serial Laue diffraction on a microfluidic crystallization device. *Journal of Applied Crystallography, 47*, 1975–1982.
79. Roedig, P., Vartiainen, I., Duman, R., Panneerselvam, S., Stube, N., Lorbeer, O., et al. (2015). A micro-patterned silicon chip as sample holder for macromolecular crystallography experiments with minimal background scattering. *Scientific Reports, 5*, 10451.
80. Roessler, C. G., Agarwal, R., Allaire, M., Alonso-Mori, R., Andi, B., Bachega, J. F., et al. (2016). Acoustic injectors for drop-on-demand serial femtosecond crystallography. *Structure, 24*, 631–640.
81. Ren, Z., Perman, B., Srajer, V., Teng, T. Y., Pradervand, C., Bourgeois, D., et al. (2001). A molecular movie at 1.8 A resolution displays the photocycle of photoactive yellow protein, a eubacterial blue-light receptor, from nanoseconds to seconds. *Biochemistry, 40*, 13788–13801.
82. Stagno, J. R., Liu, Y., Bhandari, Y. R., Conrad, C. E., Panja, S., Swain, M., et al. (2017). Structures of riboswitch RNA reaction states by mix-and-inject XFEL serial crystallography. *Nature, 541*(7636), 242–246.
83. Adams, P. D., Afonine, P. V., Bunkoczi, G., Chen, V. B., Davis, I. W., Echols, N., et al. (2010). PHENIX: A comprehensive python-based system for macromolecular structure solution. *Acta Crystallographica. Section D, Biological Crystallography, 66*, 213–221.
84. Brunger, A. T., & Rice, L. M. (1997). Crystallographic refinement by simulated annealing: Methods and applications. *Methods in Enzymology, 277*, 243–269.
85. Romo, T. D., Clarage, J. B., Sorensen, D. C., & Phillips, G. N., Jr. (1995). Automatic identification of discrete substates in proteins: Singular value decomposition analysis of time-averaged crystallographic refinements. *Proteins, 22*, 311–321.
86. Henry, E. R., & Hofrichter, J. (1992). Singular value decomposition - application to analysis of experimental-data. *Methods in Enzymology, 210*, 129–192.

87. Emsley, P., Lohkamp, B., Scott, W. G., & Cowtan, K. (2010). Features and development of coot. *Acta Crystallographica. Section D, Biological Crystallography, 66*, 486–501.
88. Murshudov, G. N., Skubak, P., Lebedev, A. A., Pannu, N. S., Steiner, R. A., Nicholls, R. A., et al. (2011). REFMAC5 for the refinement of macromolecular crystal structures. *Acta Crystallographica. Section D, Biological Crystallography, 67*, 355–367.
89. Hugonnet, J. E., Tremblay, L. W., Boshoff, H. I., Barry, C. E., 3rd, & Blanchard, J. S. (2009). Meropenem-clavulanate is effective against extensively drug-resistant *Mycobacterium tuberculosis*. *Science, 323*, 1215–1218.
90. Tremblay, L. W., Hugonnet, J. E., & Blanchard, J. S. (2008). Structure of the covalent adduct formed between Mycobacterium tuberculosis beta-lactamase and clavulanate. *Biochemistry, 47*, 5312–5316.
91. Hugonnet, J. E., & Blanchard, J. S. (2007). Irreversible inhibition of the *Mycobacterium tuberculosis* beta-lactamase by clavulanate. *Biochemistry, 46*, 11998–12004.
92. Boyd, D. B., & Lunn, W. H. (1979). Electronic structures of cephalosporins and penicillins. 9. Departure of a leaving group in cephalosporins. *Journal of Medicinal Chemistry, 22*, 778–784.
93. Deponte, D. P., McKeown, J. T., Weierstall, U., Doak, R. B., & Spence, J. C. (2011). Towards ETEM serial crystallography: Electron diffraction from liquid jets. *Ultramicroscopy, 111*, 824–827.
94. Holton, J. M., & Frankel, K. A. (2010). The minimum crystal size needed for a complete diffraction data set. *Acta Crystallographica Section D, 66*, 393–408.